Comparison of Patient-Specific Computational Modeling Predictions and Clinical Outcomes of LASIK for Myopia

Ibrahim Seven,[1] Ali Vahdati,[1] Vinicius Silbiger De Stefano,[1] Ronald R. Krueger,[2] and William J. Dupps Jr[1–3]

[1]Ocular Biomechanics and Imaging Lab, Cole Eye Institute, Cleveland Clinic, Cleveland, Ohio, United States
[2]Refractive Surgery Service, Cole Eye Institute, Cleveland Clinic, Cleveland, Ohio, United States
[3]Biomedical Engineering, Lerner Research Institute, Cleveland Clinic, Cleveland, Ohio, United States

Purpose. To assess the predictive accuracy of simulation-based LASIK outcomes.

Methods. Preoperative and 3-month post-LASIK tomographic data from 20 eyes of 12 patients who underwent wavefront-optimized LASIK for myopia were obtained retrospectively. Patient-specific finite element models were created and case-specific treatment settings were simulated. Simulated keratometry (SimK) values and the mean tangential curvature of the central 3 mm (K_{mean}) were obtained from the anterior surfaces of the clinical tomographies, and computational models were compared. Correlations between K_{mean} prediction error and patient age, preoperative corneal hysteresis (CH), and corneal resistance factor (CRF) were assessed.

Results. The mean difference for K_{mean} between simulated and actual post-LASIK cases was not statistically significant (-0.13 ± 0.36 diopters [D], $P = 0.1$). The mean difference between the surgically induced clinical change in K_{mean} and the model-predicted change was -0.11 ± 0.34 D ($P = 0.2$). K_{mean} prediction error was correlated to CH, CRF, and patient age ($r = 0.63$, 0.53, and 0.5, respectively, $P < 0.02$), and incorporation of CH values into predictions as a linear offset increased their accuracy. Simulated changes in K_{mean} accounted for 97% of the variance in actual spherical equivalent refractive change.

Conclusions. Clinically feasible computational simulations predicted corneal curvature and manifest refraction outcomes with a level of accuracy in myopic LASIK cases that approached the limits of measurement error. Readily available preoperative biomechanical measures enhanced simulation accuracy. Patient-specific simulation may be a useful tool for clinical guidance in de novo LASIK cases.

Keywords: corneal biomechanics, finite element analysis, LASIK, patient specific, validation

Laser in situ Keratomileusis (LASIK) is among the most frequently performed surgeries in the world and is associated with high global patient satisfaction rates.[1] However, LASIK and other forms of corneal refractive surgery that rely on tissue incision or removal induce corneal biomechanical changes.[2–4] These changes to the corneal structure and individual differences in the mechanical response to them are important potential drivers of residual postoperative refractive error, postoperative refractive regression, and postoperative corneal ectasia.

Although the outcomes of LASIK are among the best of any elective procedure, enhancement procedures are often required for residual or induced refractive error. Residual refractive error and the need for retreatment are significant sources of uncompensated cost, risk, and patient dissatisfaction.[1] A variety of risk factors for retreatment after primary refractive surgery have been identified, including the type and magnitude of preoperative refractive error, depth of ablation, patient age, and higher degrees of preoperative astigmatism.[5–7] In addition to the cost and intrinsic risks of additional surgery, retreatments have been associated with an increased risk of corneal ectasia.[8,9] Although historic nomograms have been useful for improving refractive outcomes through regression-based guidance of treatment offsets,[10] they are generally agnostic to individual corneal shape variations and other important drivers of the structural response to surgery. A surgical planning tool that can increase the accuracy of surgical algorithms for routine and atypical cases has the potential to reduce cost while increasing patient safety and satisfaction.

Finite element analysis (FEA)-based computational simulation is being investigated as a predictive tool to enhance clinical decision-making in an increasing number of clinical disciplines.[11] Structural analysis using the FEA method has the potential to account for the biomechanical impact of a complex three-dimensional (3D) surgical intervention while accounting for the patient's particular corneal geometric configuration and biomechanical properties. The sensitive link between the cornea's geometry, biomechanical behavior, and the optical function of the eye presents significant advantages for leveraging simulation-based engineering in keratorefractive applications. Furthermore, the cornea's accessibility with commercially available imaging systems makes creation of patient-specific models more feasible than in other tissues requiring invasive or ionizing imaging techniques.

The approach to corneal finite element modeling has progressed from homogenous material formulations[12,13] to

more microstructurally representative models[14–21] that account for preferred collagen orientations from x-ray diffraction data,[22] axially inclined collagen fibers in the anterior stroma characterized by two-photon microscopy[23] and corneal hydration behavior.[18] Only a limited number of studies have modeled the optical effects of both flap creation and ablation in the context of LASIK,[24,25] and no prior publication has performed a direct clinical comparison of computationally predicted refractive outcomes. The goal of the present study was to assess the predictive accuracy of case-specific finite element simulations of LASIK procedures through comparison to clinical topographic and refractive outcomes.

METHODS

Patient Selection and Surgery

Consecutive charts of 20 eyes of 12 subjects that underwent LASIK for myopia or myopic astigmatism on the Refractive Surgery service of the Cleveland Clinic Cole Eye Institute (Cleveland, OH, USA) and that were followed for at least 3 months after surgery were included in the study. Patients were selected by a retrospective review of corneal tomography under an institutional review board (IRB)-approved research protocol (Cleveland Clinic IRB protocol #13-213). Eyes with at least 10 mm of corneal coverage in Scheimpflug-based anterior segment scans (Pentacam HR; Oculus Optikgerate GmbH, Wetzlar, Germany) were chosen for the study from a consecutive series of refractive surgery screening candidates who had LASIK performed. Charts of patients not meeting all of these criteria were excluded. The treatments were performed by two fellowship-trained refractive surgeons (WJD, RK) using an FS200 femtosecond laser (Alcon, Fort Worth, TX, USA) or IntraLase fs60 femtosecond laser (AMO, Santa Ana, CA, USA) for flap creation and an Allegretto Eye Q 400 excimer laser system (Alcon) with a 6.5-mm optical zone in a 9-mm total ablation zone with a 1.25-mm annular transition zone. Programmed refractive correction was determined individually by each surgeon using their standard practice pattern of reviewing commercial nomogram software suggestions for each case (IBRA; Zubisoft GmbH, Oberhasli, Switzerland). As described in more detail below, case-specific surgical parameters for flap creation and excimer laser ablation were incorporated into the simulations. Only preoperative corneal tomography was used to construct computational models, and posttreatment data was used to assess model accuracy.

Corneal Anisotropy and Material Model

For modeling purposes, the cornea was represented as a nonlinear, anisotropic, hyperelastic, nearly incompressible material with depth-dependent material properties.[14,26,27] To simulate this spectrum of behavior, a microstructural fiber-reinforced material model representing collagen fibers was combined with an isotropic Neo-Hookean solid extrafibrillar matrix to produce a composite corneal stroma.[28–30] Collagen crimping behavior was accounted for by representing each collagen fibril as a 3D spring proposed by Freed et al.[28,29] where H is the axial distance between two turns of the helix, R is the radius of the helix, and r is the radius of the fiber thickness. The microstructural helical spring model requires three parameters: Ho/Ro (the ratio between initial axial distance between two turns within the helix and the initial radius of the helix), Ro/ro (the initial radius of the helix and the radius of the fiber thickness), and Ef (the elastic modulus of the fiber when it is uncrimped and behaves in its linear

region).[15,28] The resulting fiber behavior was calculated using the algorithm given elsewhere by Freed et al.[29]

Corneal material strength is dependent on stromal fiber distributions and their preferred orientations.[22,31–33] The material formulation proposed by Freed et al.[29] was limited to reflect this behavior in the fiber splay. Therefore, the algorithm was combined with the equation given by Pinsky et al.[15] to more realistically simulate the corneal stroma (Equations 1–4). At each integration point within the model, splay of fibers was modeled and angularly integrated to represent a gradual change in fiber orientation from the center to the periphery of cornea. The equations are partially reproduced here to demonstrate how fiber and matrix components are accounted for in the total strain energy density function (Equation 1) and how the fiber component is defined using the probability density function (Φ) to describe the presence of fiber population as a function of rotational angle (θ) and radial distance from the corneal center (R) (Equations 2–4). The separate treatment of fiber orientation for central (Equation 3) and peripheral (Equation 4) cornea allows representation of the transition from predominantly orthogonal to more circumferential/tangential orientation near the limbus. A linear combination of Equations 3 and 4 was used in the transition zone between central and peripheral regions. The details of the components of this equation including n, c_1, and c_2 were explained by Pinsky et al.[15]

$$W = W_{\text{isotropic}} + W_{\text{fiber}} + W_{\text{volumetric}} \qquad (1)$$

$$W_{\text{fiber}} = \frac{1}{\pi} \int_0^\pi \Phi(R_{\text{cornea}}, \varphi; \theta) W_{\text{fibril}}(R, \varphi; \theta)\, d\theta \qquad (2)$$

$$\Phi(R_{\text{cornea}}, \phi; \theta) = \cos^{2n}(\theta) + \sin^{2n}(\theta) + c_1$$
$$0 < R_{\text{cornea}} < 4.5\,\text{mm} \qquad (3)$$

$$\Phi(R_{\text{cornea}}, \phi; \theta) = \sin^{2n}(\theta - \phi) + c_2$$
$$4\,\text{mm} < R_{\text{cornea}} < 5.5\,\text{mm} \qquad (4)$$

Depth-dependent properties of the cornea were simulated by linearly scaling the ground matrix material constant, C_{10}, in the material model down to 50% from anterior to posterior regions of the stroma to approximate experimental data in human corneal explants.[34] The material model was implemented in an Abaqus v611 UMAT subroutine (Dassault Systemes Simulia Corp., Providence, RI, USA).[30] The pretreatment corneal material constants were obtained by performing an inverse FEA[30] on previously published experimental inflation and tensile test data from a 50-year-old excised human cornea.[35] This analysis produced material constants that were then used in the models to represent the normative preoperative stroma. Preoperative material constants were defined as follows: the shear modulus of isotropic ground matrix $C_{10} = 0.04$ MPa, the compressibility constant $D = 0.0001$ MPa^{-1}, the ratio of the axial length of the collagen fibers spring to the diameter of the collagen fiber $H_0 r_0 = 30.5$, the unitless ratio of radial diameter of the collagen fiber to the diameter of the collagen fiber $R_0 r_0 = 1.51$, and the elastic modulus of the collagen fibers $Ef = 32$ MPa. Epithelium was modeled as a uniformly thick 50-μm isotropic hyperelastic neo-Hookean material. The shear modulus of the epithelium was set as 1% of the shear modulus of the stroma, and the fiber component was omitted due to absence of continuous collagen elements and the epithelium's negligible contribution to the corneal structural response.
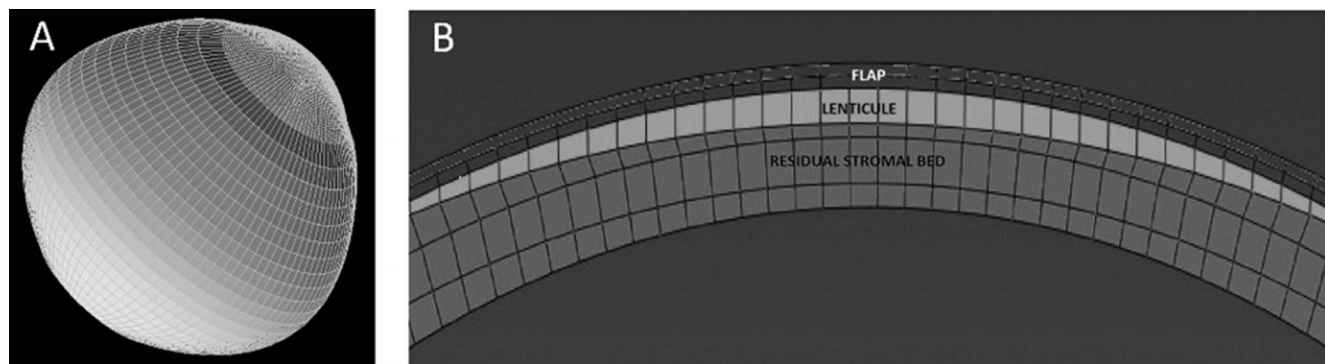
FIGURE 1. (**A**) Representative side-view of cornea-scleral finite element mesh. (**B**) Representative cross-section of a corneal mesh to demonstrate myopic LASIK correction applied to the cornea with LASIK flap, ablated lenticule, and residual stromal bed.

Model Generation

Patient-specific preoperative Cartesian coordinates of the anterior and the posterior surfaces were exported from Pentacam as grid format comma separated value files. The data were interpolated and meshed with eight-node hexahedral brick elements (Fig. 1A) with SpecifEye v0.1 (Optoquest, Cleveland, OH, USA).[20] The preoperative geometry was divided into four regions in depth (Fig. 1B): epithelium (50 μm), stromal component of the flap (50 μm), flap interface wound (10 μm), and posterior stroma (defined as the remaining patient-specific thickness).[36] A generic sclera, with an anterior thickness matched to the patient-specific peripheral corneal thickness, was generated to form the posterior portion of the eye in order to capture the effects of limbal displacement within the simulation.[20,24] The posterior surface of the corneoscleral globe was then subjected to a homogenous IOP of 15 mm Hg.

Surgical Simulation and Stress-Free Geometry Calculation

Myopia with astigmatism treatments were simulated with their patient-specific treatment settings recorded in operation reports. These treatment settings were translated from the spectacle plane to the corneal plane.[37] The patients received wavefront optimized treatments. The ablation profile calculation and equations were given by Mrochen et al.[37] Finite element analysis were run using a commercial FEA solver Abaqus v6.11 (Dassault Systemes Simulia Corp.). The amount of ablation was calculated for each node in the 3D finite element model and the nodes were repositioned according to their ablation magnitudes in the geometry with a custom Python script. Because the corneal Scheimpflug scans were acquired under physiological IOP, the stress-free geometries were calculated by an iterative technique given elsewhere by Pandolfi et al.[14,38] and modified by our group.[25,39] The corneal surface coordinates of the unoperated mesh (X_0) depend on the patient specific tomographies acquired under pressure. The nodal coordinates of the mesh within the treatment zone were modified from X_{pre} to X_{post} according to the ablation algorithm. The coordinates of the postoperative mesh (including the treatment zone and the peripheral cornea, limbus, and sclera) were taken as a reference (X_{ref}). A negative pressure with amplitude 90% lower than the physiologic IOP (15 mm Hg) was applied to the posterior surface of the postoperative corneoscleral model (X_{ref}). The displacements that were calculated from the negative pressure ($u_{deflation}$) were added to X_{ref} to obtain the initial set of coordinates (X_0) to start the iterative no-load calculation (Equation 5). Following the

deflation, the physiologic IOP (15 mm Hg) was iteratively applied and error (e) was calculated as the root mean square (RMS) of the distances between the nodes in the whole corneoscleral structure from the reference and the calculated geometries (Euclidian norm). The iterations were stopped once RMS error was less than 1×10^{-5}, which typically required six or seven iterations.

$$X_0 = X_{ref} + u_{deflation} \qquad (5)$$

The wound region peripheral to the flap was simulated to represent the restored strength resulting from healing at the femtosecond laser interfaces. The width of the wound region was defined as 305° arc (360° minus hinge width of 55°) with a 10-μm thickness.[40] The side cut was simulated with a 50% weakening in the isotropic component and omitting the fiber component of the strain energy equation (Equation 6). The flap was simulated by omitting the fiber component of the strain energy equation (Equation 7).[36] All patients were operated on using a circular flap with 9-mm diameter and 90° side cut angle. Hinge width was reported as 55° for all patients at 12 o'clock position. All simulations conformed to these reported surgical parameters for each patient.

A wound region beneath the flap was also defined in the model. This region was simulated by a 90% weakening of the isotropic region and omitting the fiber component from the strain energy equation (Equation 8) to approximate the cohesive weakening measured in ex vivo post-LASIK corneas.[41] The material properties of the posterior cornea remained unchanged for the LASIK simulation.

$$W_{cutwound} = 0.5 \times W_{isotropic} + W_{volumetric} \qquad (6)$$

$$W_{flap} = W_{isotropic} + W_{volumetric} \qquad (7)$$

$$W_{wound} = 0.1 \times W_{isotropic} + W_{volumetric} \qquad (8)$$

Data Analysis

Following the simulations, anterior corneal surface coordinates of pre- and posttreatment geometries were exported from Abaqus Version 6.11 (Dassault Systemes Simulia Corp.). Using the pre- and posttreatment anterior surface coordinates from both simulated and clinical geometries, simulated K values including mean tangential curvature from the central 3-mm region (K_{mean}), the average curvature of the steepest meridian (K_1), and the average curvature of the flattest meridian (K_2) of the anterior corneal surface were calculated. Tangential curvature at each point (K_{tan}) on the cornea was calculated using the first and second derivative of an 8th order Zernike fit

TABLE 1. Comparison of Anterior Curvature Values for Pre-LASIK Clinical Cases and Modeled Pre-LASIK Geometries for Model Verification

Patient	Clinical					Model					Model–Clinical				
	K_1	K_2	K_1–K_2	Angle	K_{mean}	K_1	K_2	K_1–K_2	Angle	K_{mean}	ΔK_1	ΔK_2	$\Delta(K_1$–$K_2)$	ΔAngle	ΔK_{mean}
1	44.94	44.35	0.59	119	44.55	44.91	44.27	0.64	115	44.55	−0.03	−0.08	0.05	−4	0
2	44.88	44.76	0.12	42	44.67	44.87	44.50	0.37	68	44.67	−0.01	−0.26	0.25	26	0
3	43.10	42.24	0.86	96	42.48	43.29	42.42	0.87	95	42.48	0.19	0.18	0.01	−1	0
4	43.27	42.24	1.03	106	42.63	43.42	42.47	0.95	103	42.63	0.15	0.23	−0.08	−3	0
5	42.08	41.31	0.77	107	41.60	42.00	41.23	0.77	110	41.59	−0.08	−0.08	0.00	3	−0.01
6	41.77	41.26	0.51	55	41.49	41.63	41.24	0.39	60	41.49	−0.14	−0.02	−0.12	5	0
7	42.29	41.98	0.31	51	42.23	42.51	42.06	0.45	58	42.23	0.22	0.08	0.14	7	0
8	43.95	42.67	1.28	98	43.16	43.91	42.67	1.24	98	42.66	−0.04	0.00	−0.04	0	−0.50
9	44.35	43.83	0.52	128	44.06	44.26	43.64	0.62	118	44.05	−0.09	−0.19	0.10	−10	−0.01
10	43.16	42.19	0.97	170	42.67	43.33	42.44	0.89	165	42.67	0.17	0.25	−0.08	−5	0
11	43.38	42.19	1.19	167	42.76	43.48	42.44	1.04	170	42.76	0.10	0.25	−0.15	3	0
12	45.24	43.66	1.58	96	44.36	45.46	43.72	1.74	98	44.35	0.22	0.06	0.16	2	−0.01
13	44.29	43.89	0.40	73	43.97	44.22	43.68	0.54	71	43.97	−0.07	−0.21	0.14	−2	0
14	42.56	41.36	1.20	153	42.04	42.46	41.33	1.13	148	42.04	−0.10	−0.03	−0.07	−5	0
15	43.16	41.87	1.29	27	42.43	43.01	41.77	1.24	27	42.43	−0.15	−0.10	−0.05	0	0
16	45.00	44.18	0.82	78	44.73	45.17	44.29	0.88	79	44.73	0.17	0.11	0.06	1	0
17	42.67	42.13	0.54	99	42.38	42.76	42.09	0.67	97	42.37	0.09	−0.04	0.13	−2	−0.01
18	42.24	42.19	0.05	166	42.19	42.33	42.25	0.08	115	42.18	0.09	0.06	0.03	−51	−0.01
19	43.38	42.67	0.71	99	43.05	43.63	42.85	0.78	95	43.05	0.25	0.18	0.07	−4	0
20	43.05	42.78	0.27	74	42.87	43.25	42.97	0.28	84	42.87	0.20	0.19	0.01	10	0
Mean											0.06	0.03	0.03	−1.5	−0.03
SD											±0.14	±0.16	±0.11	±13.9	±0.11
P											0.08	0.4	0.3	0.6	0.3

All curvatures are expressed in diopters and angle is in degrees. K_1, average curvature of the steepest meridian; K_2, average curvature of the flattest meridian; K_1-K_2, anterior corneal astigmatism; angle: orientation of the anterior surface astigmatism in degrees; K_{mean}, average tangential curvature within central 3-mm region.

(Z) of the anterior corneal surface with respect to distance from the center of the cornea (r_{cornea}) (Equation 9). The constants of Zernike polynomials (Z) were calculated with a linear regression analysis using a custom Python script. The calculated tangential curvature values were converted to diopters (D) using Snell's law with a corneal refractive index of 1.3375 (the keratometric index, which estimates the total corneal power assessed at the anterior corneal surface). Pretreatment clinical K_1 and K_2 values were directly taken from Pentacam tomographies for comparison. Pretreatment model, posttreatment clinical, and simulated K_1 and K_2 values were calculated using SpecifEye. The pairwise differences of these variables for clinical and simulated geometries were calculated. Statistical significance was determined by paired Student's *t*-tests for nonindependent samples with *P* less than 0.05 indicating significance (MINITAB, Minitab, Inc., State College, PA, USA).

$$K_{tan} = \frac{\left(1 + \left(\frac{dZ}{dr_{cornea}}\right)^2\right)^{3/2}}{\left|\frac{d^2Z}{dr_{cornea}^2}\right|} \qquad (9)$$

Corneal hysteresis (CH) and corneal resistance factor (CRF) obtained at each preoperative screening exam with the Ocular Response Analyzer (ORA; Reichert Ophthalmic Instruments, Buffalo, NY, USA) were recorded. Correlations between these variables and the difference in predicted versus actual curvature values were investigated using Pearson correlation. Programmed change in central anterior corneal curvature was calculated as the spherical equivalent (SE) of the programmed correction following the vertex calculation with a 12.5-mm vertex distance. Actual and simulated changes were calculated by subtracting preoperative K_{mean} from postoperative K_{mean} for actual and simulated cases, respectively. Treatment and

prediction errors were calculated as differences between actual – programmed changes and predicted – actual changes, respectively.

RESULTS

The mean patient age averaged across eyes was 39.3 ± 12.7 years. Clinical tomographic characteristics of the simulated eyes included a mean maximum curvature (maximum K) of 44.12 ± 1.21 D (mean ± SD), mean apical corneal thickness of 570.5 ± 21.9 μm, and mean minimum corneal thickness of 568.1 ± 21.7 μm.

The mean programmed refraction correction was −3.18 ± 1.69 D for the spherical component and −0.50 ± 0.35 D for the cylindrical component. Tables 1 and 2 show individual K_1, K_2, corneal astigmatism (K_1–K_2), steep axis, and K_{mean} values and comparisons of actual and simulation values for the preoperative and post-LASIK states, respectively. Preoperative model fidelity was verified by comparing each value from clinical tomography to that of the associated finite element model, and none of the differences were statistically significant. The mean difference in K_{mean} (ΔK_{mean}) between actual outcomes of the surgeries and the predictions produced by their corresponding LASIK simulations was not statistically significant (−0.13 ± 0.36 D, *P* = 0.1 by paired Student's *t*-test). The only statistically significant difference between clinical and simulated values across the preoperative and postoperative comparisons was for K_2 (+0.13 ± 0.28 D, *P* = 0.03). Errors in the agreement of the axis of steep astigmatism were also insignificant and were higher in individual cases with very low magnitudes of astigmatism where axis identification (both by refraction and by keratometric analysis) is anticipated to be error prone but of minimal clinical consequence.

TABLE 2. Comparison of Absolute Curvature Values for Post-LASIK Clinical Cases and Post-LASIK Models

Patient	Clinical					Model					Model–Clinical				
	K_1	K_2	$K_1–K_2$	Angle	K_{mean}	K_1	K_2	$K_1–K_2$	Angle	K_{mean}	ΔK_1	ΔK_2	$\Delta(K_1–K_2)$	ΔAngle	ΔK_{mean}
1	41.93	41.17	0.76	137	41.71	42.28	41.25	1.03	142	41.60	0.35	0.08	0.27	5	−0.11
2	41.45	41.22	0.23	132	41.46	42.50	41.68	0.82	28	41.86	1.05	0.46	0.59	−104	0.40
3	40.52	40.34	0.18	67	40.29	40.89	40.52	0.37	83	40.56	0.37	0.18	0.19	16	0.27
4	40.68	40.49	0.19	129	40.51	40.82	40.38	0.44	109	40.47	0.14	−0.11	0.25	−20	−0.04
5	39.45	39.24	0.21	44	39.40	39.42	39.35	0.07	165	39.20	−0.03	0.11	−0.14	121	−0.20
6	39.56	39.05	0.51	143	39.46	39.23	39.05	0.18	117	38.95	−0.33	0.00	−0.33	−26	−0.51
7	36.60	36.46	0.14	178	37.11	37.50	36.89	0.61	81	37.03	0.90	0.43	0.47	−97	−0.08
8	42.78	42.39	0.39	99	42.92	42.59	42.22	0.37	40	42.34	−0.19	−0.17	−0.02	−59	−0.58
9	37.59	36.77	0.82	169	37.46	37.31	36.82	0.49	96	36.98	−0.28	0.05	−0.33	−73	−0.48
10	39.99	39.82	0.17	81	40.11	40.48	40.30	0.18	99	40.16	0.49	0.48	0.01	18	0.05
11	39.91	39.53	0.38	105	40.04	40.48	40.30	0.18	99	40.25	0.57	0.77	−0.20	−6	0.21
12	44.12	42.03	2.09	104	42.72	43.47	41.92	1.55	99	42.63	−0.65	−0.11	−0.54	−5	−0.09
13	36.61	36.12	0.49	64	36.59	37.44	36.72	0.72	89	36.99	0.83	0.60	0.23	25	0.40
14	38.10	37.93	0.17	2	38.62	37.98	37.82	0.16	74	37.60	−0.12	−0.11	−0.01	72	−1.02
15	39.82	39.53	0.29	62	39.95	39.61	39.56	0.05	61	39.39	−0.21	0.03	−0.24	−1	−0.56
16	43.77	42.68	1.09	85	43.17	43.31	42.43	0.88	79	42.86	−0.46	−0.25	−0.21	−6	−0.31
17	39.00	38.45	0.55	82	38.90	39.20	38.36	0.84	90	38.72	0.20	−0.09	0.29	8	−0.18
18	39.52	39.01	0.51	94	39.23	39.43	39.13	0.30	89	39.20	−0.09	0.12	−0.21	−5	−0.03
19	42.41	41.23	1.18	99	41.70	42.06	41.28	0.78	96	41.62	−0.35	0.05	−0.40	−3	−0.08
20	41.59	40.65	0.94	84	41.16	41.74	41.19	0.55	75	41.33	0.15	0.54	−0.39	−9	0.17
Mean											0.11	0.13	−0.01	−7.4	−0.13
SD											±0.48	±0.28	±0.31	±52.8	±0.36
P											0.3	0.03	0.6	0.5	0.1

The right side of the table indicates differences between clinical results and model-based predictions. Negative prediction errors indicate a flatter curvature prediction (relative overcorrection).

To address the possibility of statistical error from the inclusion of both eyes of some patients, we performed a correlation analysis of the prediction error (ΔK_{mean}) between right and left eyes of the eight patients who had both eyes enrolled. The analysis suggested no significant intraclass correlation ($r = 0.11$, $P = 0.95$). The minimum detectable difference for K_{mean} was 0.23 D for a paired *t*-test using values $n = 20$, $\alpha = 0.05$, and $\beta = 0.2$ (80% statistical power) by post-hoc calculation. All predicted K_{mean} values were within 1.00 D of the clinical postoperative value, with 55%, 85%, and 95% of the cases demonstrating prediction errors within 0.25, 0.50, and 0.75 D, respectively (Fig. 2). Figure 2 also presents a prediction error frequency based on an adjustment for preoperative biomechanical measurement and is further described below.

Figures 3, 4, and 5 illustrate the case-specific prediction error in K_{mean} expressed as a function of CRF, CH, and age. Forty percent of the variance in K_{mean} prediction error was accounted for by interindividual differences in preoperative CH. Twenty-nine percent was accounted for by CRF, and 25%
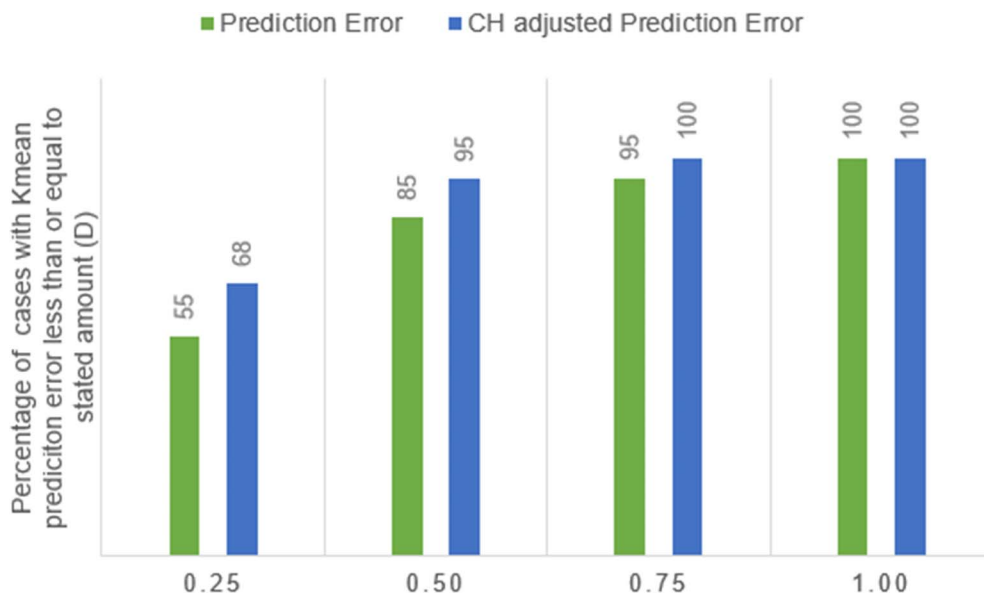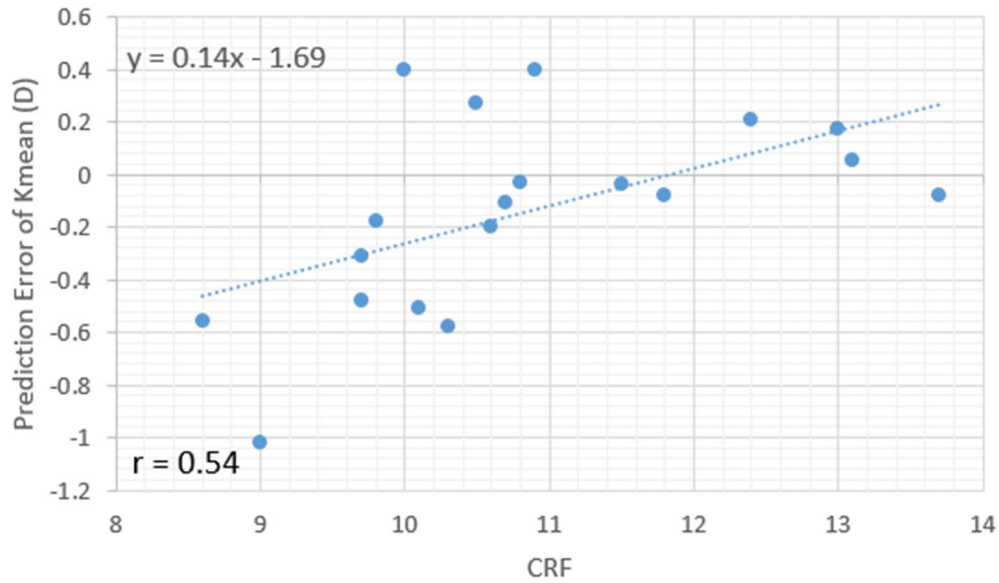

FIGURE 2. Percentage of cases with less than or equal to 0.25, 0.50, 0.75, and 1.00 D of error in the actual versus predicted anterior tangential curvature of the central 3 mm (K_{mean}, D). *Green*: prediction error, *Blue*: CH-adjusted prediction error.

FIGURE 3. Scatterplot and linear regression of the case-specific prediction error in mean central corneal curvature (D) as a function of preoperative corneal resistance factor (CRF, mm Hg) indicating a trend toward overestimation of myopic correction in subjects with lower CRF.

by age ($P = 0.016$, 0.004, and 0.02, respectively). ΔK_{mean} values were confirmed to be normally distributed, and a one-sided outlier analysis using Grubbs' test for the null hypothesis that all data points come from the same normally distributed population did not suggest that the largest prediction error, -1.02 D, was a statistical outlier ($P = 0.08$). When the linear regression equation for the strongest preoperative predictor of prediction error (CH) was used as a linear adjustment to the model-predicted curvature, the magnitude and frequency of observed error improved (Fig. 2).

Table 3 reports attempted, actual, and predicted changes in central corneal curvature (K_{mean}) and assesses treatment error and prediction errors. The treatment error, expressed as the difference between programmed refractive change calculated at the anterior corneal plane and actual change in K_{mean}, was statistically significant ($+0.40 \pm 0.30$ D, $P < 0.05$). However,

the model prediction error in K_{mean} was not statistically significant (-0.11 ± 0.34 D, $P = 0.2$).

Table 4 shows the value for pre- and postoperative manifest refraction for each patient, as well as the model-predicted curvature change and the vertex-corrected change after LASIK. The Pearson correlation coefficient for these last two variables is high ($P = 0.99$) and the scatterplot graph (Fig. 6) also demonstrates a strong correlation between predicted changes in corneal curvature and corneal vertex–corrected changes in actual SE manifest refraction.

DISCUSSION

LASIK is one of the world's most commonly performed procedures and is associated with high levels of patient satisfaction.[1] Surgeons frequently use personal nomograms or
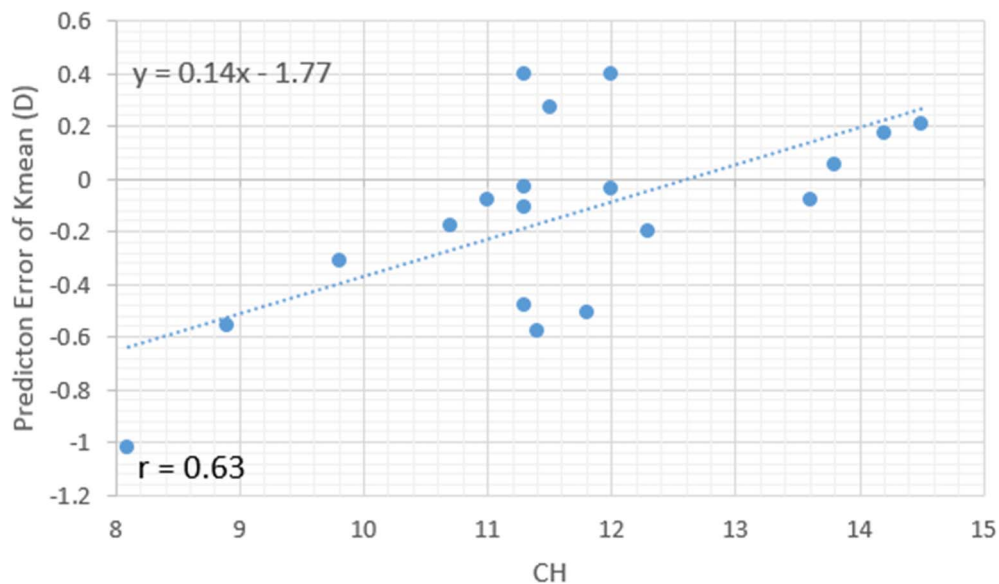
FIGURE 4. Scatterplot and linear regression of the case-specific prediction error in mean central corneal curvature (D) as a function of preoperative corneal hysteresis (CH, mm Hg) indicating a trend toward overestimation of myopic correction in subjects with lower CH.
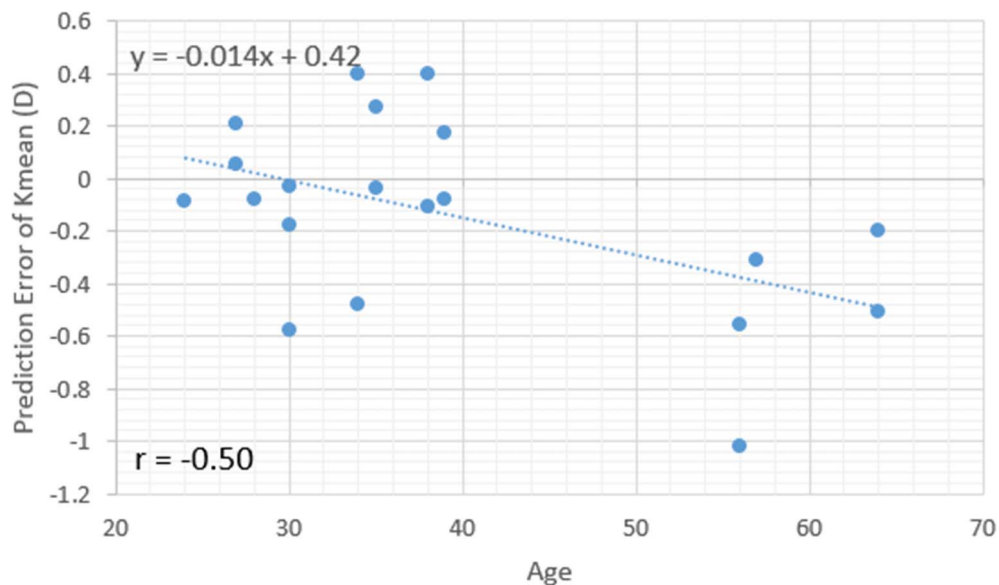
FIGURE 5. Scatterplot and linear regression of the case-specific prediction error in mean central corneal curvature (D) as a function of age (years) indicating a trend toward overestimation of myopic correction in older subjects.

commercial software-based equivalents as a guide for modifying the laser input to reduce the risk of outcome variability. Although planning systems vary in complexity, the process involves entry of a small number of patient- and surgery-specific variables, interrogation of a regression formula developed from historic outcome data as a function of some subset of those inputs, and generation of a predicted refractive outcome and/or suggested treatment entry for generating the desired correction. These tools have been an important part of outcomes analysis and optimization since the inception of corneal refractive surgery, and analogous methods are also widely used in incisional keratotomy, intraocular lens calculation, intracorneal ring implantation, and other forms of ocular surgery.

TABLE 3. Accuracy of Predicted LASIK Outcomes Expressed as the Change in Anterior Tangential Corneal Curvature Averaged Over the Central 3 mm (K_{mean})

| Patient	Programmed SE Refractive Change at Corneal Plane, D	Clinical K_{mean} Change, D	Model-Predicted K_{mean} Change, D	Difference in Programmed SE Change and Clinical K_{mean} Change	Model Prediction Error in K_{mean}
1	−3.24	−2.84	−2.95	0.40	−0.11
2	−3.01	−3.21	−2.81	−0.21	0.40
3	−2.43	−2.19	−1.92	0.24	0.27
4	−2.66	−2.12	−2.16	0.53	−0.04
5	−2.54	−2.20	−2.39	0.34	−0.19
6	−2.67	−2.03	−2.54	0.63	−0.51
7	−5.58	−5.12	−5.20	0.46	−0.08
8	−0.63	−0.24	−0.32	0.39	−0.08
9	−7.48	−6.60	−7.07	0.87	−0.47
10	−2.89	−2.56	−2.51	0.32	0.05
11	−2.89	−2.72	−2.51	0.17	0.21
12	−1.95	−1.64	−1.72	0.31	−0.08
13	−7.48	−7.38	−6.98	0.10	0.40
14	−4.60	−3.42	−4.44	1.18	−1.02
15	−3.24	−2.48	−3.04	0.76	−0.56
16	−1.95	−1.56	−1.87	0.39	−0.31
17	−3.94	−3.48	−3.65	0.45	−0.17
18	−3.25	−2.96	−2.98	0.28	−0.02
19	−1.71	−1.35	−1.43	0.36	−0.08
20	−1.83	−1.71	−1.54	0.12	0.17
Mean				0.40	−0.11
SD				±0.30	±0.34
P				<0.05	0.2

Programmed SE refractive change, SE of the clinically programmed refractive treatment calculated at the corneal vertex; clinical K_{mean} change, difference between clinical post- and pre-LASIK K_{mean} values; model-predicted K_{mean} change, difference between post- and pre-LASIK K_{mean} from the computational model, treatment error (difference between actual and attempted change); model prediction error in K_{mean}, difference between simulated and actual change in K_{mean}.

TABLE 4. Comparison of Model-Predicted Outcomes Expressed as the Change in Anterior Tangential Corneal Curvature Averaged Over the Central 3 mm (K_{mean}) and the Actual Vertex-Corrected SE Change in Manifest Refraction, Calculated Using the Difference Between Pre- and Post-Operative SE and Assuming Vertex Distance of 12.5 mm

Patient	Preoperative Manifest Refraction SE, D	Post-Operative Manifest Refraction SE, D	Model-Predicted K_{mean} Change, D	Vertex-Corrected SE Change, D	Difference in Predicted Change, D
1	−3.63	−0.25	−2.95	−3.24	0.29
2	−3.63	0.00	−2.81	−3.47	0.66
3	−2.50	−0.13	−1.92	−2.31	0.39
4	−2.75	0.00	−2.16	−2.66	0.50
5	−2.63	0.00	−2.39	−2.54	0.15
6	−3.00	0.00	−2.54	−2.89	0.35
7	−6.25	−0.25	−5.20	−5.58	0.38
8	−0.75	0.00	−0.32	−0.74	0.42
9	−8.25	−0.25	−7.07	−7.27	0.20
10	−3.13	0.25	−2.51	−3.24	0.73
11	−3.00	0.00	−2.51	−2.89	0.38
12	−1.75	0.00	−1.72	−1.71	−0.01
13	−8.25	−0.50	−6.98	−7.07	0.09
14	−4.50	−0.13	−4.44	−4.15	−0.29
15	−5.00	−1.50	−3.04	−3.35	0.31
16	−2.00	0.00	−1.87	−1.95	0.08
17	−4.25	0.00	−3.65	−4.04	0.39
18	−3.13	0.00	−2.98	−3.01	0.03
19	−1.25	0.13	−1.43	−1.35	−0.08
20	−1.25	−0.13	−1.54	−1.11	−0.43
Mean			−3.00	−3.23	0.23
SD			±1.74	±1.75	±0.29
Pearson's ρ			0.99 ($P < 0.001$)		

Nomogram-based guidance accounts for several sources of systematic variability using a retrospective, empirical fit to the response data. However, there are limitations to a probabilistic approach. Regression models are fit to the average response and typically intersect only a minority of the actual responses. Regression models are historic in nature and optimized for the data used to fit the model; predictive performance beyond the range of previous observations and in prospective forecasting involves additional uncertainty.[42] The variables represented in nomograms are sparse representations of the patient and the procedure and do not leverage potentially predictive 3D corneal tomography datasets. The statistical associations
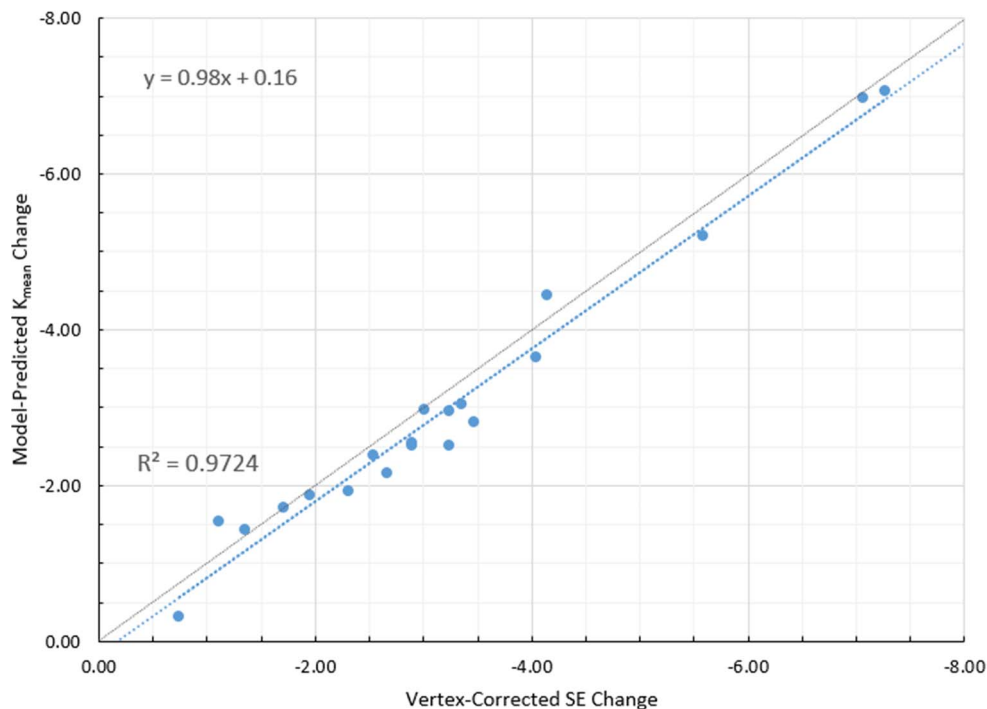
FIGURE 6. Scatterplot and linear regression comparing case-specific predictions of mean central corneal curvature (K_{mean}) change to actual change in vertex-corrected SE manifest refraction.

produced by regression models do not explicitly reflect the biophysical mechanisms of variability and are therefore of limited utility for de novo inferences in complex or atypical cases. Also, aside from surrogate associations related to patient age, nomograms do not explicitly account for the biomechanical impact of the intervention on corneal geometry and optical outcome.[2,4,26]

In this study, we investigated the ability of a computational modeling method that directly incorporates patient-specific 3D corneal geometry, case-specific treatment geometry, and evidence-based corneal anisotropy and depth-dependent material property assumptions to simulate actual clinical LASIK outcomes. While previous studies have suggested a role for finite element modeling in enhancing the predictability of refractive surgery procedures by accounting for intrinsic patient characteristics and the biomechanical nature of the surgery,[24,36,43] the current study is the first to assess the predictive performance of a model in a series of keratorefractive surgery patients. This is a critical step in assessing computational modeling as a potential clinical decision support tool in the surgical planning process.

The comparison of model predictions and clinical outcomes was performed in a series of cases with myopic LASIK corrections as high as 8.25 D (SE) and up to 1.50 D of refractive astigmatism, and conclusions about predictive performance should be limited to the range of refractive errors assessed in the current study. The mean pairwise difference in central anterior corneal curvature (K_{mean}) derived from each computational model from the same metric measured in the actual post-LASIK tomographies—an absolute comparison of predictive accuracy—was insignificant (-0.13 ± 0.36 D, $P = 0.1$). In relative terms, the mean difference between the surgically induced clinical change in K_{mean} and the model-predicted change was also insignificant (-0.11 ± 0.34 D, $P = 0.2$). The keratometric variable K_{mean} was selected as the primary outcome measure because it was thought to represent the most optically important changes within a typical photopic entrance pupil and because the data directly represent the input and output of the modeling process. However, to relate the predictive performance of the model more directly to clinical refractive outcomes, a direct comparison of predicted changes in model K_{mean} to the vertex-adjusted SE manifest refractive change was performed and produced close agreement across the range of corrections (Table 4; Fig. 6) with a mean error of $+0.23 \pm 26$ D. While K_{mean} considers only corneal first-surface changes in curvature, simulation results compared favorably with subjective manifest refraction results that depend on whole-eye optics. Ray tracing analysis is being incorporated into the modeling software to account for additional sources of refractive change such as axial length and posterior corneal surface changes.

Overall, the differences between the model predictions and clinical outcomes were statistically insignificant and within the precision limits of topographic measurement and clinical refraction (±0.25 D) for most cases. When the clinical error in achieved versus programmed K_{mean} change (0.40 ± 0.30 D) was compared with the prediction error in the same metric (-0.11 ± 0.34 D), the ranges of clinical and prediction error were comparable. However, the model prediction was closer in magnitude to the actual K_{mean} change than the programmed correction by a factor of 4. Individual comparisons of these differences in Table 3 suggest that preoperative adjustments to the surgical plan based on case-specific model predictions would potentially have improved treatment accuracy in 16 of 20 cases. The actual programmed correction for each case was used to drive each associated simulation and included any spherical and/or cylindrical treatment offsets incorporated by the surgeon after reviewing commercial nomogram software output.

The analysis of model prediction error as a function of preoperative air-puff–derived biomechanical metrics is the first to directly associate the predictability of LASIK outcomes with these variables. The case with the largest discrepancy between programmed and achieved change in K_{mean} (an apparent 1.18-D myopic undercorrection) and also the largest prediction error in K_{mean} (-1.08 D) also had the lowest preoperative CH value. While CH is not a measure of the corneal elastic modulus, the trend toward undercorrection of myopia in eyes with lower CH and overcorrection in those with higher CH reflects earlier FEA-based sensitivity analyses suggesting greater anterior displacement of the residual stromal bed and thus myopic undercorrection in eyes with lower corneal stiffness properties.[44] For simulation purposes, every patient was assumed to have identical, normative initial material properties at the anterior stroma. The isotropic component of these properties were then reduced as a function of depth as described in the methods, and thus produced different depth-dependent property profiles due to differing patient-specific corneal thicknesses. However, the absence of knowledge regarding actual patient-specific material properties is a potential source of prediction error in these simulations, and the finding that a linear adjustment for CH could improve prediction fidelity is important evidence that incorporation of individual measures of corneal properties in the future could enhance model performance. On average, the models predicted slightly flatter corneas than were observed in actual cases, and this could be due to a slightly stiff corneal material assumption.

Another important source of variance in the simulations is the test–retest repeatability of the corneal surface elevation data derived from clinical tomography scans. The current study suggests that a high level of predictive fidelity can be achieved even within the context of a typical clinical workflow involving capture of a single preoperative scan. Selection of optimal scans from a set of replicate measurements may support even stronger predictive performance, and improvements in repeatability with OCT-based tomography methods[45,46] coupled with the ability of emerging OCT and high-frequency ultrasound devices to generate patient-specific epithelial thickness maps[47] will provide even greater opportunities for improved model accuracy.

In summary, a clinically feasible approach to computational simulations predicted corneal curvature and manifest refraction outcomes with a high level of accuracy in myopic LASIK cases. An automated workflow for the steps described in this study is in place to allow software-driven tomography file transfer and treatment data entry, cloud-based finite element analysis simulation, and electronic delivery of simulation results in under 30 minutes with the goal of providing a useful tool for clinical guidance in de novo LASIK cases.

References

1. Solomon KD, Fernandez de Castro LE, Sandoval HP, et al. LASIK world literature review: quality of life and patient satisfaction. *Ophthalmology*. 2009;116:691–701.

2. Jaycock PD, Lobo L, Ibrahim J, et al. Interferometric technique to measure biomechanical changes in the cornea induced by refractive surgery. *J Cataract Refract Surg*. 2005;31:175–184.

3. Krueger RR, Dupps WJ Jr. Biomechanical effects of femtosecond and microkeratome-based flap creation: prospective contralateral examination of two patients. *J Refract Surg*. 2007;23:800–807.

4. Dupps WJ Jr, Roberts C. Effect of acute biomechanical changes on corneal curvature after photokeratectomy. *J Refract Surg*. 2001;17:658–669.

5. Hersh PS, Fry KL, Bishop DS. Incidence and associations of retreatment after LASIK. *Ophthalmology*. 2003;110:748–754.

6. Randleman JB, White AJ Jr, Lynn MJ, et al. Incidence, outcomes and risk factors for retreatment after wavefront-optimized ablations with PRK and LASIK. *J Refract Surg*. 2009;25:273–276.

7. Mimouni M, Vainer I, Shapira Y, et al. Factors predicting the need for retreatment after laser refractive surgery. *Cornea*. 2016;35:607–612.

8. Rani A, Murthy BR, Sharma N, et al. Posterior corneal topographic changes after retreatment LASIK. *Ophthalmology*. 2002;109:1991–1995.

9. Randleman JB, Russell B, Ward MA, et al. Risk factors and prognosis for corneal ectasia after LASIK. *Ophthalmology*. 2003;110:267–275.

10. Yuen LH, Chan WK, Koh J, et al. A 10-year prospective audit of LASIK outcomes for myopia in 37,932 eyes at a single institution in Asia. *Ophthalmology*. 2010;117:1236–1244.e1.

11. National Science Foundation. Simulation-Based Engineering Science: Revolutionizing Engineering Science through Simulation. Arlington, VA, May 2006. Available at: https://www.nsf.gov/pubs/reports/sbes_final_report.pdf.

12. Bryant MR, McDonnell PJ. Constitutive laws for biomechanical modeling of refractive surgery. *J Biomech Eng*. 1996;118:473–481.

13. Elsheikh A, Wang D, Kotecha A, et al. Evaluation of Goldmann applanation tonometry using a nonlinear finite element ocular model. *Ann Biomed Eng*. 2006;34:1628–1640.

14. Pandolfi A, Holzapfel GA. Three-dimensional modeling and computational analysis of the human cornea considering distributed collagen fibril orientations. *J Biomech Eng*. 2008;130:061006.

15. Pinsky P, van der Heide D, Chernyak D. Computational modeling of mechanical anisotropy in the cornea and sclera. *J Cataract Refract Surg*. 2005;31:136–145.

16. Petsche SJ, Pinsky PM. The role of 3-D collagen organization in stromal elasticity: a model based on X-ray diffraction data and second harmonic-generated images. *Biomech Model Mechanobiol*. 2013;12:1101–1113.

17. Petsche SJ, Chernyak D, Martiz J, et al. Depth-dependent transverse shear properties of the human corneal stroma. *Invest Ophthalmol Vis Sci*. 2012;53:873–880.

18. Cheng X, Petsche SJ, Pinsky PM. A structural model for the in vivo human cornea including collagen-swelling interaction. *J R Soc Interface*. 2015;12:20150241.

19. Seven I, Dupps WJ. Patient-specific finite element simulations of standard incisional astigmatism surgery and a novel patterned collagen crosslinking approach to astigmatism treatment. *J Med Dev*. 2013;7:0409131–0409132.

20. Seven I, Sinha Roy A, Dupps WJ Jr. Patterned corneal collagen crosslinking for astigmatism: computational modeling study. *J Cataract Refract Surg*. 2014;40:943–953.

21. Whitford C, Studer H, Boote C, et al. Biomechanical model of the human cornea: considering shear stiffness and regional variation of collagen anisotropy and density. *J Mech Behav Biomed Mater*. 2015;42:76–87.

22. Meek K, Quantock A. The use of X-ray scattering techniques to determine corneal ultrastructure. *Prog Retin Eye Res*. 2001;20:95–137.

23. Winkler M, Shoa G, Xie Y, et al. Three-dimensional distribution of transverse collagen fibers in the anterior human corneal stroma. *Invest Ophthalmol Vis Sci*. 2013;54:7293–7301.

24. Roy AS, Dupps WJ Jr. Effects of altered corneal stiffness on native and postoperative LASIK corneal biomechanical behavior: a whole-eye finite element analysis. *J Refract Surg*. 2009;25:875–887.

25. Roy AS, Dupps WJ Jr. Patient-specific computational modeling of keratoconus progression and differential responses to collagen cross-linking. *Invest Ophthalmol Vis Sci*. 2011;52:9174–9187.

26. Dupps WJ Jr, Wilson SE. Biomechanics and wound healing in the cornea. *Exp Eye Res*. 2006;83:709–720.

27. Pinsky PM, van der Heide D, Chernyak D. Computational modeling of mechanical anisotropy in the cornea and sclera. *J Cataract Refract Surg*. 2005;31:136–145.

28. Freed A, Doehring T. Elastic model for crimped collagen fibrils. *J Biomech Eng*. 2005;127:587–593.

29. Freed A, Einstein D, Vesely I. Invariant formulation for dispersed transverse isotropy in aortic heart valves - an efficient means for modeling fiber splay. *Biomech Model Mechanobiol*. 2005;4:100–117.

30. Vahdati A, Seven I, Mysore N, et al. Computational biomechanical analysis of asymmetric ectasia risk in unilateral post-LASIK ectasia. *J Refract Surg*. In press.

31. Meek KM, Boote C. The use of X-ray scattering techniques to quantify the orientation and distribution of collagen in the corneal stroma. *Prog Retin Eye Res*. 2009;28:369–392.

32. Boote C, Elsheikh A, Kassem W, et al. The influence of lamellar orientation on corneal material behavior: biomechanical and structural changes in an avian corneal disorder. *Invest Ophthalmol Vis Sci*. 2011;52:1243–1251.

33. Boote C, Hayes S, Abahussin M, Meek K. Mapping collagen organization in the human cornea: left and right eyes are structurally distinct. *Invest Ophthalmol Vis Sci*. 2006;47:901–908.

34. Randleman JB, Dawson DG, Grossniklaus HE, et al. Depth-dependent cohesive tensile strength in human donor corneas: implications for refractive surgery. *J Refract Surg*. 2008;24:S85–S89.

35. Elsheikh A, Wang D, Brown M, et al. Assessment of corneal biomechanical properties and their variation with age. *Curr Eye Res*. 2007;32:11–19.

36. Sinha Roy A, Dupps WJ Jr, Roberts CJ. Comparison of biomechanical effects of small-incision lenticule extraction and laser in situ keratomileusis: finite-element analysis. *J Cataract Refract Surg*. 2014;40:971–980.

37. Mrochen M, Donitzky C, Wullner C, Loffler J. Wavefront-optimized ablation profiles: theoretical background. *J Cataract Refract Surg*. 2004;30:775–785.

38. Elsheikh A, Whitford C, Hamarashid R, et al. Stress free configuration of the human eye. *Med Eng Phys*. 2013;35:211–216.

39. Seven I, Dupps WJ. Patient-specific finite element simulations of standard incisional astigmatism surgery and a novel patterned collagen crosslinking approach to astigmatism treatment. *J Med Device*. 2013;7:409131–409132.

40. Dawson DG, Kramer TR, Grossniklaus HE, et al. Histologic, ultrastructural, and immunofluorescent evaluation of human

laser-assisted in situ keratomileusis corneal wounds. *Arch Ophthalmol*. 2005;123:741–756.

41. Schmack I, Dawson DG, McCarey BE, et al. Cohesive tensile strength of human LASIK wounds with histologic, ultrastructural and clinical correlations. *J Refract Surg*. 2005;21:433–445.

42. Geisser S. *Predictive Inference: An Introduction*. New York, NY: Chapman & Hall; 1993.

43. Sanchez P, Moutsouris K, Pandolfi A. Biomechanical and optical behavior of human corneas before and after photorefractive keratectomy. *J Cataract Refract Surg*. 2014;40:905–917.

44. Sinha Roy A, Dupps WJ Jr. Effects of altered corneal stiffness on native and postoperative LASIK corneal biomechanical behavior: a whole-eye finite element analysis. *J Refract Surg*. 2009;25:875–887.

45. McNabb RP, Farsiu S, Stinnett SS, et al. Optical coherence tomography accurately measures corneal power change from laser refractive surgery. *Ophthalmology*. 2015;122:677–686.

46. Lanza M. Re: McNabb et al.: Optical coherence tomography accurately measures corneal power change from laser refractive surgery (Ophthalmology 2015;122:677–86). *Ophthalmology*. 2016;123:e5–e6.

47. Reinstein DZ, Archer TJ, Gobbe M. Change in epithelial thickness profile 24 hours and longitudinally for 1 year after myopic LASIK: three-dimensional display with Artemis very high-frequency digital ultrasound. *J Refract Surg*. 2012;28:195–201.